Solar Energy Materials & Solar Cells 238 (2022) 111579

Contents lists available at ScienceDirect

Solar Energy Materials and Solar Cells

journal homepage: www.elsevier.com/locate/solmat

Laboratory intercomparison of solar absorptance and thermal emittance measurements at room temperature

Simon Caron [a,*], Leslie Herding [b], Yaniv Binyamin [c], Mubeen Baidossi [c], Yelena Vinetsky [d], Angel Morales [e], Christina Hildebrandt [f], Reine Reoyo-Prats [g], Olivier Faugeroux [g], Alina Agüero [h], Sergio Rodriguez [h], Florian Sutter [a], Marc Röger [a], Francisco Manzano-Agugliaro [i]

[a] Institute of Solar Research, German Aerospace Center (DLR), Paseo de Almería 73-2, 04001 Almería, Spain
[b] Institute for Research in Technology (IIT), ICAI School of Engineering, Universidad Pontificia Comillas, C/Santa Cruz de Marcenado 26, 28015 Madrid, Spain
[c] Brightsource Industries, 11 Kiryat Mada St., Amot Building n°6, P.O. Box 45220, Har Hotzvim, 91450, Jerusalem, Israel
[d] Institute of Chemistry, The Hebrew University of Jerusalem, Jerusalem, 9190401, Israel
[e] CIEMAT-PSA, Materials for Concentrating Solar Thermal Technologies Unit, Avenida Complutense 40, Madrid 28040, Spain
[f] Fraunhofer Institut für Solare Energiesysteme (ISE), Heidenhofstr. 2, 79110, Freiburg, Germany
[g] Laboratoire Procédés et Matériaux pour l'Energie Solaire (PROMES-UPR CNRS 8521), Technosud, Rambla de la Thermodynamique, 66100, Perpignan, France
[h] Instituto Nacional de Técnica Aeroespacial (INTA), Ctra. de Ajalvir km.4, 28850, Torrejón de Ardoz, Spain
[i] Department of Engineering, CEIA3, University of Almería, 04120, Almería, Spain

ARTICLE INFO

Keywords:
Concentrated solar power
Solar thermal
Absorber coating
Solar absorptance
Thermal emittance

ABSTRACT

Solar thermal absorber coatings play an important role in the opto-thermal efficiency of receivers in Concentrated Solar Power (CSP). Two standard figures of merit are the solar absorptance α_{sol} and thermal emittance ε_{th}, derived from spectral directional hemispherical reflectance measurements at room temperature. These two figures of merit allow comparing coating formulations in terms of performance and durability.

In this study, a black coating and a solar selective coating are optically characterized by different laboratories to compare spectral datasets, solar absorptance α_{sol} and thermal emittance ε_{th} calculations. The comparison includes various benchtop spectrophotometers operating in the UV-VIS-NIR and Infrared spectral ranges as well as three commercial portable reflectometers/emissometers.

A good agreement is found between the nine parties participating in this intercomparison campaign. The black coating α_{sol} value is 96.6 ± 0.2%, while the solar selective coating α_{sol} value is 94.5 ± 0.4%. For the thermal emittance, spectral data is concatenated and integrated from 0.3 to 16 μm. The black coating ε_{th} value calculated at 650 °C is 80.8 ± 3.8%, while the solar selective coating ε_{th} value calculated at 650 °C is 25.0 ± 0.5%.

1. Introduction

Concentrated Solar Power (CSP) technologies coupled to thermal storage can provide fossil-free electricity, process heat or synthetic fuels around the clock at a competitive price, especially in sunniest regions of the globe [1–4]. CSP technologies use a mirror field to concentrate Direct Normal Irradiance (DNI) on a thermal receiver. A Heat Transfer Fluid (HTF) absorbs the heat and transports it to a thermodynamic process. Four types of mirror field configurations are typically identified for CSP technologies, i.e. parabolic troughs [5,6], solar towers, also known as Central Receiver Systems (CRS) [7,8], Linear Fresnel [9] and Dish systems [10].

One key component for any CSP technology is the thermal receiver. Tubular receiver designs are most common among commercial plants. Parabolic trough and Linear Fresnel receivers consist of an absorber tube inserted in an evacuated glass envelope, while solar towers use external tubular bundle heat exchanger designs, with several parallel absorber tubes assembled in panels. The absorber tube is made of a metal substrate, for instance stainless steel or a nickel-based alloy, on which a Solar Thermal Absorber Coating (STAC) is applied. The typical absorber operating temperature ranges from 300 to 600 °C for parabolic troughs and solar towers using molten salt as a HTF [11,12]. For solar towers, allowable flux density constraints have to be considered to avoid HTF freezing below 300°C or pronounced corrosion above 600 °C [13,14].

The STAC opto-thermal performance is characterized by two key

* Corresponding author.
E-mail address: simon.caron@dlr.de (S. Caron).

https://doi.org/10.1016/j.solmat.2022.111579
Received 29 July 2021; Received in revised form 4 December 2021; Accepted 31 December 2021
Available online 19 January 2022

Nomenclature

Abbreviations

AM	Air Mass
ASTM	American Society for Testing Materials
CERMET	Ceramic Metallic
CSP	Concentrated Solar Power
D&S	Devices and Services
DNI	Direct Normal Irradiance
DTGS	Deuterated Triglycine Sulfate
FTIR	Fourier Transform Infrared
HTF	Heat Transfer Fluid
HSA	High Solar Absorptance
ISO	International Organization for Standardization
IR	Infrared
MCT	Mercure Cadmium Telluride
NIR	Near Infrared
NIST	U.S. National Institute of Standards and Technology
NPL	U.K. National Physical Laboratory
SDHR	Spectral Directional Hemispherical Reflectance
SOC	Surface Optics
SSC	Solar selective coating
STAC	Solar thermal absorber coating
TNO	Netherlands Organization for Applied Scientific Research
UV	Ultraviolet
VIS	Visible

Participants

CIEMAT	Centro de Investigaciones Energeticas, Medioambientales y Technologicas
CNRS	Centre National de la Recherche Scientifique
DLR	Deutsches Zentrum für Luft- und Raumfahrt
HUJI	Hebrew University of Jerusalem
ISE	Institute for Solar Energy Systems
INTA	Instituto Nacional de Técnica Aeroespacial
OPAC	Joint CIEMAT-DLR optical laboratory at PSA
PROMES	Procédés et Matériaux pour l'Energie Solaire
PSA	Plataforma Solar de Almeria

English Symbols

C_x	Concentration ratio[-]
d	Direct + circumsolar[-]
g	Global[-]
I	Intensity[-]
T	Coating temperature[°C, K]
$\dot{q}''_{sol}$	Concentrated solar flux[W.m^{-2}]
Z	Trade-off factor[-]

Greek Symbols

α_{sol}	Solar absorptance[%]
ε_{th}	Thermal emittance[%]
Λ	Wavelength[μm]
$\eta_{opt\text{-}th}$	Opto-thermal efficiency[%]
P	Reflectance[%]
Θ	Incidence angle[°]

figures of merit [15], i.e. solar absorptance α_{sol} and thermal emittance ε_{th} , both measurable according to international standards [16–23]. High Solar Absorptance (HSA) coatings [24–27] maximize primarily the solar absorptance α_{sol}, while Solar Selective Coatings (SSC) [28–31] also minimize the thermal emittance ε_{th}. The selection of an absorber coating formulation depends on the optimization of the coating opto-thermal efficiency [32,33], considering coating durability [24,25,34–38] in order to minimize the levelized cost of coating (LCOC) [38,39].

New STAC formulations have been developed within the EU project Raiselife [41] and their durability has been tested [42–44]. In this paper, we compare α_{sol} and ε_{th} measurements made at room temperature in different laboratories. On the one hand, both measurements are important to compare new coating formulations in pristine state. On the other hand, these measurements are also relevant to measure deviations with respect to the pristine state and thus track any optical coating degradation that may occur during durability test campaigns. Measurements at operating temperature have been discussed previouslyin the literature [45–50] for similar coatings and are here considered out of scope for this laboratory intercomparison.

The laboratory intercomparison includes both benchtop spectrophotometers and a few commercial portable devices. While spectrophotometers provide a fine spectral resolution, Fourier Transform Infrared (FT-IR) spectrophotometers typically require a cryogenic cooling of the detector. Meanwhile, portable devices have a limited spectral resolution, but allow performing a coating inspection on site. The intercomparison is here outlined for two reference STAC, i.e. one HSA black coating and one SSC, which have been exchanged between participating laboratories.

The measurement protocol is first explained, describing the instrumentation set for optical measurements, the set of reference samples and the equations for processing spectral measurements. Spectral data is then compared, discussing spectral mismatch between optical instruments. Solar absorptance and thermal emittance calculations are then analyzed, introducing some variants for the weighting, for instance air mass or infrared spectral range. Finally, the propagation of uncertainty on the opto-thermal efficiency is discussed.

Table 1
List of participants.

Participant	Location	Role
Brightsource Industries	Jerusalem, Israel	Sample preparation (x2) Measurement
CIEMAT	Madrid, Spain	Measurement
CIEMAT-DLR (OPAC, PSA)	Plataforma Solar de Almeria Tabernas, Spain	Measurement Evaluation
DLR	Cologne, Germany	Measurement
Fraunhofer ISE	Freiburg, Germany	Sample preparation (x2) Measurement
HUJI	Jerusalem, Israel	Measurement
INTA	Madrid, Spain	Measurement
PROMES-CNRS	Perpignan, France	Measurement
OMT Solutions B.V.	Eindhoven, Netherlands	Calibration

2. Materials and methods

2.1. Organization and participants

This laboratory intercomparison test campaign involved 9 participants from 5 countries (France, Germany, Israel, Netherlands and Spain). Participating laboratories are listed in Table 1 and their location is shown on Fig. 1. Four reference flat samples, further described in Section 2.3, were prepared for this campaign. Brightsource Industries and Fraunhofer Institute for Solar Energy Systems (ISE) respectively applied their STAC on two flat samples.

For each STAC, one sample was submitted to OMT Solutions B.V [51]. for an independent calibration against NIST traceable standards.

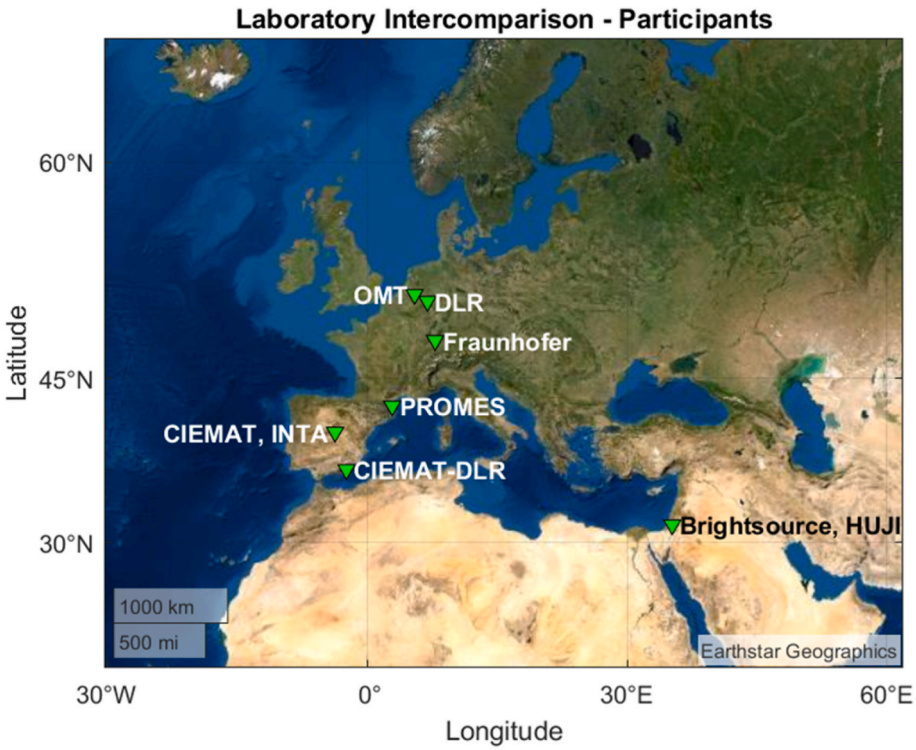

Fig. 1. Laboratory intercomparison – location of participants.

Table 2
Inventory of measurement instruments.

	UV-VIS-NIR (≤ 2.5 µm)			Infrared (> 1.5 µm)		
Participant	*Spectro photometer?*	*Portable device ?*	*Device Model*	*Spectro photometer?*	*Portable device ?*	*Device Model*
Brightsource Industries	-	✓	SOC 410-Solar	-	✓	SOC ET-100
CIEMAT	✓	-	Perkin Elmer Lambda 950	✓	-	Perkin Elmer Frontier FTIR
CIEMAT-DLR (OPAC, PSA)	✓	-	Perkin Elmer Lambda 1050	✓	-	Perkin Elmer Frontier FTIR
DLR	✓	-	Perkin Elmer Lambda 1050	-	-	N.A.
Fraunhofer ISE	✓	-	Bruker Vertex 80	✓	-	Bruker Vertex 80
HUJI	✓	-	Agilent Cary 5000	-	✓	Devices &Services AE1/RD1
INTA	✓	-	Agilent Cary 5000	-	✓	AZ Technology Temp2000A
PROMES-CNRS	✓	-	Perkin Elmer Lambda 950	✓	-	SOC 100 HDR + Nicolet 6700 FTIR
OMT Solutions	✓	-	Perkin Elmer Lambda 1050	✓	-	Perkin Elmer 983 IR

These calibrated samples were then returned to OPAC laboratory, a joint CIEMAT-DLR cooperation, at the Plataforma Solar de Almería (PSA) in Tabernas, Spain. Meanwhile, the other samples circulated between participating laboratories, except OMT Solutions. After this laboratory intercomparison test campaign, these samples were stored at OPAC laboratory. Each participant submitted its processed dataset obtained after instrument calibration to CIEMAT-DLR for evaluation.

2.2. Instrumentation

For each participating laboratory, measurement instruments are listed in Table 2. Each participant uses two optical measurement instruments to characterize α_{sol} and ε_{th} at room temperature. These measurement instruments operate in complementary spectral ranges, i.e. UV-VIS-NIR from ~ 0.3 to 2.5 µm, relevant for α_{sol}, and the infrared range above 2.5 µm, most relevant for ε_{th}.

Table 3
Comparison of spectral ranges reported in raw spectral datasets.

Participant	Spectral range [μm]		Spectral resolution [nm]	
	UV-VIS-NIR	*Infrared*	*UV-VIS-NIR*	*Infrared*
Brightsource Industries	[0.335–2.5]	[1.5–21]	7 bands	6 bands
CIEMAT	[0.25–2.5]	[2.5–16]	10 nm	~ 2 nm
CIEMAT-DLR (OPAC, PSA)	[0.28–2.5]	[2.0–16]	5 nm	4 nm
DLR	[0.28–2.5]	N.A.	5 nm	N.A.
Fraunhofer ISE	[0.32–2.4]	[1.5–16]	2.5 nm	~ 4 nm
HUJI	[0.28–2.5]	[2–50]	1 nm	Broadband
INTA	[0.25–2.5]	[3–35]	1 nm (<0.8 μm) 2 nm (>0.8 μm)	Broadband
PROMES-CNRS	[0.25–2.5]	[1.5–25]	10 nm	Variable
OMT Solutions	[0.22–2.51	[1.66–21.6]	5 nm	Variable

Brightsource Industries is the only participant to use a portable device for both measurements, namely the SOC 410-VIS-IR modular solar reflectometer/emissometer, developed by Surface Optics [52], which combines two measurement heads (410-Solar [53] and ET-100 [54]). This portable device can be transported in the field to measure α_{sol} and ε_{th} on flat and tubular samples.

Four participants use two benchtop spectrophotometers, i.e. CIEMAT, CIEMAT-DLR, Fraunhofer ISE and PROMES-CNRS. Fraunhofer ISE is the only participant using a single benchtop instrument (Bruker Vertex 80) to cover the full spectral range. In the UV-VIS-NIR spectral range, a PerkinElmer Lambda 950 or 1050 spectrophotometer is used by four participants, i.e. CIEMAT, DLR, PROMES-CNRS and OMT Solutions. In the infrared range, CIEMAT and CIEMAT-DLR both use a PerkinElmer Frontier Fourier FTIR spectrophotometer, while PROMES-CNRS uses a SOC 100 HDR model.

INTA and HUJI adopt an alternative approach: both use a benchtop spectrophotometer (Agilent, Cary 500/5000), in the UV-VIS-NIR range for α_{sol} measurements, while they use a portable emissometer (AZ Technology, Temp2000A [55,56] and D&S, AE1/RD1 [57,58] for ε_{th} measurements.

Measurement spectral ranges and resolutions are detailed for each participant in Table 3 and displayed in Fig. 2 a. on a logarithmic scale, while spectral bands of the SOC portable device are detailed in Fig. 2 b. The spectral resolution reported by each participant for benchtop spectrophotometers is shown in Fig. 3 as a function of wavelength. It corresponds to the wavelength steps reported by each participant for raw spectral measurements.

The common spectral range of interest for UV-VIS-NIR measurements is defined from 0.3 to 2.5 μm, while infrared measurements are provided at least until 16 μm. For the SOC portable device and some benchtop spectrophotometers, a spectral overlap exists between 1.5 and 2.5 μm (Brightsource Industries, CIEMAT-DLR, Fraunhofer ISE, PROMES-CNRS, OMT Solutions).

For benchtop spectrophotometers, a constant spectral resolution is observed for UV-VIS-NIR measurements, ranging from 1 to 10 nm, while the spectral resolution is variable for Infrared measurements. This is partly explained by the instrument optical setup, i.e. UV-VIS-NIR spectrophotometers typically use a monochromator to sample light at different wavelengths, while FTIR spectrophotometers typically use an interferometer and their spectral resolution is often defined in wavenbumber (cm-1), which translate in a variable wavelength step. For

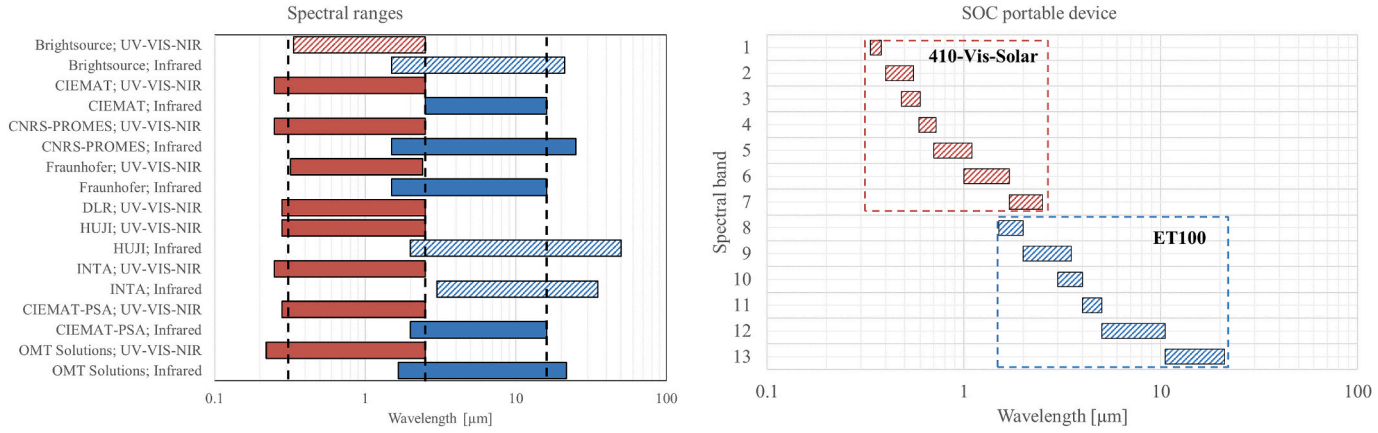

Fig. 2. Comparison of spectral ranges a) Overview b) SOC portable device spectral bands.

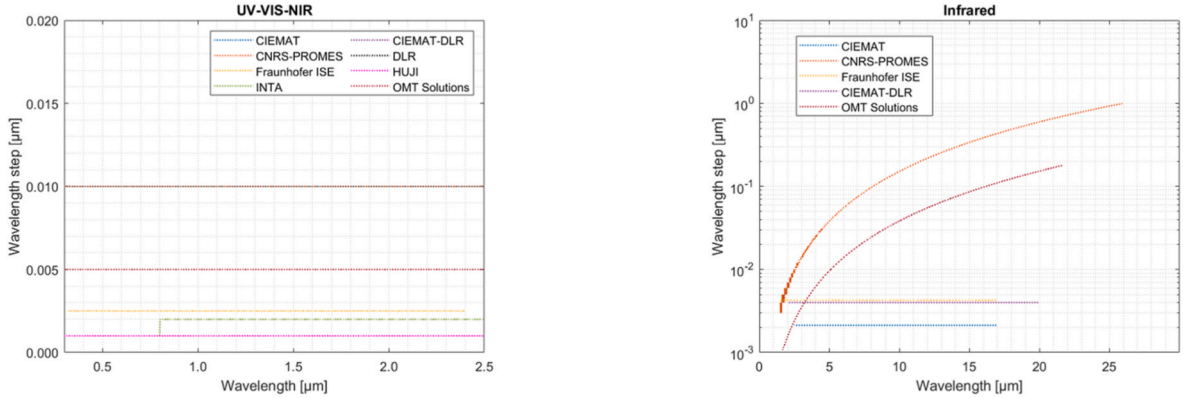

Fig. 3. Comparison of spectral ranges for benchtop spectrophotometers.

Table 4
UV-VIS-NIR instrument specifications.

Participant	Light source	Detector(s)	Integrating sphere
Brightsource Industries	Tungsten filament	7 spectral bands	θ: 20°; Ø: N.A.
CIEMAT	UV: Deuterium VIS-NIR: Tungsten Halogen	InGaAs & PbS; Peltier cooling	θ: 8°; Ø: 150 mm white, diffuse
CIEMAT-DLR (OPAC, PSA)	UV: Deuterium VIS-NIR: Tungsten Halogen	InGaAs & PbS; Peltier cooling	θ: 8°; Ø: 150 mm white, diffuse
DLR	UV: Deuterium VIS-NIR: Tungsten Halogen	InGaAs & PbS; Peltier cooling	θ: 8°; Ø: 150 mm white, diffuse
Fraunhofer ISE	UV: Deuterium VIS-NIR: Tungsten	Photomultipliers Si & InGaAs diodes	θ: 8°; Ø: 200 mm white, diffuse
HUJI	UV: Deuterium VIS-NIR: Tungsten Halogen	InGaAs & PbS; Peltier cooling	θ: 8°; Ø: 150 mm white, diffuse
INTA	UV: Deuterium VIS-NIR: Tungsten Halogen	InGaAs & PbS; Peltier cooling	θ: 8°; Ø: 150 mm white, diffuse
PROMES-CNRS	UV: Deuterium VIS-NIR: Tungsten Halogen	InGaAs & PbS; Peltier cooling	θ: 8°; Ø: 150 mm white, diffuse

Table 5
Infrared instrument specifications.

Participant	Light source	Detector	Integrating sphere
Brightsource Industries	IR filament	6 spectral bands 1.5–5 μm: PbSe, Peltier Cooling 5–21 μm: DTGS	θ: 20°; Ø: N.A.
CIEMAT	IR filament	Detector: MCT Liquid nitrogen cooling	θ: 12°; Ø: 76.2 mm Gold, diffuse
CIEMAT-DLR (OPAC, PSA)	IR filament	Detector: MCT Liquid nitrogen cooling	θ: 12°; Ø: 76.2 mm Gold, diffuse
Fraunhofer ISE	IR filament (glowbar)	Detector: MCT Liquid nitrogen cooling	θ: 8°; Ø: 200 mm Gold, diffuse
HUJI	Electrical heated detector	Broadband detector	N.A., Ø: 57 mm
INTA	Heated cavity	Pyroelectric detector	N.A.
PROMES-CNRS	IR filament	Detector: DTGS	θ: 8°; Adjustable [8–80°] Ø: N.A.

further analysis, spectral datasets are interpolated with a 1 nm wavelength step.

Further instrumentation details related to the light source, detector type and integrating sphere are respectively listed in Table 4 for the UV-VIS-NIR spectral range and in Table 5 for the infrared range. Pictures of benchtop spectrophotometers and portable instruments are respectively shown in Fig. 4 and Fig. 5.

2.3. Reference and calibration samples

Four flat absorber samples were prepared for this test campaign. The metal substrate is made of ferrensitic/martensitic steel T91/P91 and the sample size is 50 × 50 mm. Two samples were coated with a black coating, while two samples were coated with a SSC. One sample of each coating is shown in Fig. 6. The black coating is applied on a sand blasted substrate, while the SSC is applied on a polished substrate.

One sample of each coating was submitted to OMT Solutions for calibration, using NIST traceable calibration coupons as a baseline, respectively a white diffuse sample for the UV-VIS-NIR spectral range and a gold diffuse or specular sample for the infrared spectral range. Spectral data is shown on Fig. 7 for samples calibrated by OMT Solutions as well as commercially available calibrated sample coupons, i.e. white diffuse Spectralon® (99% reflectance) and gold diffuse Infragold® [59].

These reference calibrated sample coupons exhibit a nearly constant spectral response in the range of interest and thus can be approximated as gray bodies. The black coating shows on the one hand a nearly flat and low reflectance in the UV-VIS-NIR spectral range and on the other hand a variable response in the infrared range, while the SSC spectrum approaches a sigmoid profile, with a low reflectance in the UV-VIS-NIR range and a high reflectance asymptote in the infrared range.

Available measurement datasets are listed in Table 6. The black samples could be measured by all participating laboratories, while the SSC sample could not be measured in the UV-VIS-NIR range by HUJI and DLR (Cologne) due to technical issues. Infrared measurements could not be performed at DLR Cologne as no instrument was available for this measurement.

Reference samples used for baseline measurements are listed in Table 7 for each participant. It is worth mentioning that Fraunhofer ISE does not perform baseline measurements. Different baseline samples may be used to measure the black coating and the SSC, considering whether the surface is diffuse (black coating) or specular (SSC). These baseline samples are traceable to primary standards calibrated by reference laboratories (NIST, OMT Solutions, TNO, NPL).

2.4. Optical characterization

Applicable standards for benchtop spectrophotometers using integrating spheres are ISO 22973:2014 [16], ISO 16378:2013 [17] or ASTM E903:2020 [18]. For portable devices, ASTM C1549:2016 [19] is applicable for solar absorptance, while ASTM C1371:2015 [20] or ASTM E408:2013 [21] apply for portable emissometers. In this section, the processing of spectral data is outlined further for benchtop spectrophotometers.

2.4.1. Spectral processing

Benchtop spectrophotometers measure the spectral directional hemispherical reflectance (SDHR) for any sample, using an integrating sphere. For all spectrophotometers, except for the FTIR measurement at Fraunhofer ISE, a background (spectrum are first recorded. A reference sample (Table 7) is then mounted on the integrating sphere sample port and its SDHR is measured as a baseline. This sample is then removed and replaced by the material to be measured. Knowing the zeroline $I_{zero,\ meas}$, the baseline calibrated reflectance $\rho_{ref,calib}$, the baseline and reference sample measured intensities $I_{base,\ meas}$ and $I_{sample,\ meas}$, one derives the sample reflectance $\rho_{sample,SDHR}$ applying (Eq. (1)). This reflectance is measured for a wavelength λ (Table 3), at a near normal incidence angle θ (8–12°) (Table 4 - Table 5), at room temperature (T ~ 20–25 °C).

$$\rho_{sample,SDHR}(\lambda,\theta,T)=\frac{I_{sample,meas}-I_{zero}}{I_{base,meas}-I_{zero}}.\rho_{ref,calib} \quad (1)$$

For the FTIR spectrometer at Fraunhofer ISE a different procedure is

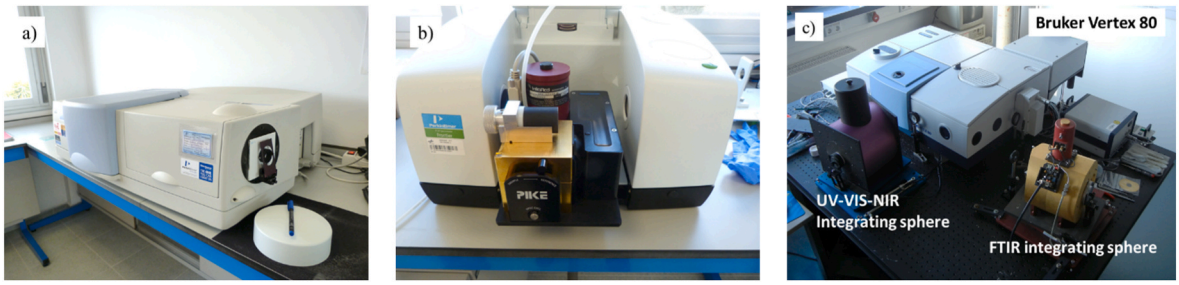

Fig. 4. Benchtop spectrophotometers a) PerkinElmer Lambda 1050 b) PerkinElmer Frontier FTIR with Pike Ltd integrating sphere (upward sample positioning). c) Bruker Vertex 80 with.

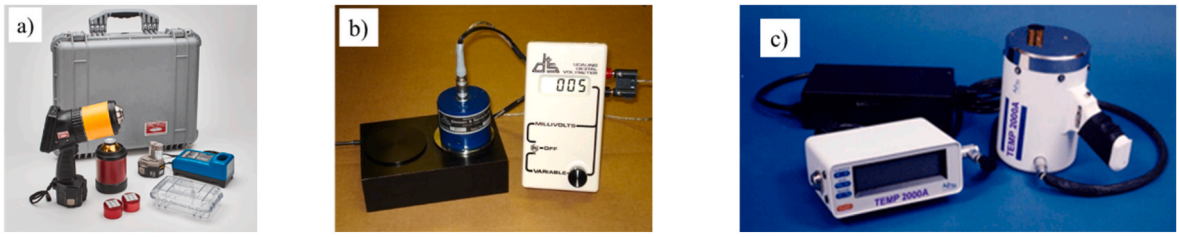

Fig. 5. Portable reflectometers and emissometers. a) SOC 410-Vis-IR portable solar reflectometer and emissometer, b) Devices and Services AE1/RD1 c) AZ Technology Temp 2000A.

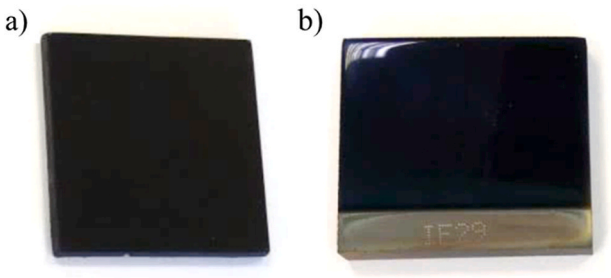

Fig. 6. Flat coated samples a) Black coating b) SSC.

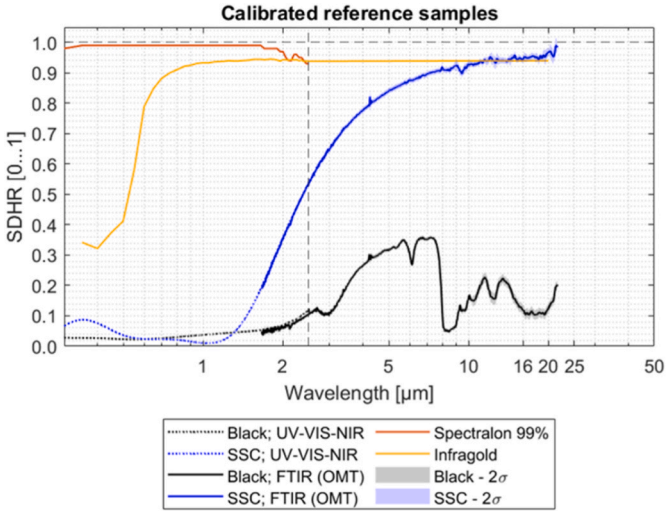

Fig. 7. Spectral directional hemispherical reflectance (SDHR) of calibrated reference samples, including 2σ spectral uncertainty bands in the infrared range for black and SSC calibrated reference samples.

applied. A calibration is done every 3 months approximately using the reference coupon cited in Table 7. In a sample measurement, we measure the reference (which is either the diffuse wall of the UV/VIS integrating sphere or a gold IR-mirror within the IR integrating sphere) and sample in alternating minute intervals. The mean value of the measurements is formed and the measurement is corrected with the respective calibration curve from the calibration.

Sample reflectance is assumed to remain stable for any wavelength at higher temperature (Eq. (2)). Measurements at higher temperature require more sophisticated instrumentation [22,23,45,46], experimental data for other similar absorber coatings has been previously published [47–50].

$$\frac{d\rho_{sample}(\lambda,\theta,T)}{dT} \backsim 0 \tag{2}$$

The spectral deviation between both spectrophotometers is calculated according to (Eq. (3)), using interpolated spectral data with a 1 nm wavelength step. The common interval for comparison between CIEMAT-DLR, Fraunhofer ISE, CNRS-PROMES and OMT-Solutions ranges from 2 to 2.5 μm. In this interval, spectral mismatch statistics (average, standard deviation) are derived according to (Eq. (3)).

$$\Delta\rho(\lambda) = \rho_{sample,FTIR}(\lambda) - \rho_{sample,UV-VIS-NIR}(\lambda) \tag{3}$$

For further calculations, available experimental spectral data is concatenated, considering UV-VIS-NIR measurements until 2.5 μm and then infrared measurements above 2.5 μm.

2.4.2. *Spectral weighting*

The solar absorptance α_{sol} is calculated for each reference sample, weighting the sample reflectance $\rho_{sample,corr}$ with a reference solar spectrum according to (Eq. (4)). The common integration interval is defined from $\lambda_1 = 0.3$ to $\lambda_2 = 2.5$ μm. The reference solar spectrum G_{sol} (λ,AM) is defined according to ASTM G173-03 [60] derived from SMARTS v2.9.2 [61]. Three spectra are considered for the comparison, i. e. extraterrestrial (Air Mass AM0), AM1.5 global and direct + circumsolar, AM1.5.

Table 6
Inventory of measurement datasets.

	Black coating		Solar selective coating	
Participant	*UV-VIS-NIR*	*Infrared*	*UV-VIS-NIR*	*Infrared*
Brightsource Industries	✓	✓	✓	✓
CIEMAT (Madrid)	✓	✓	✓	✓
CIEMAT-DLR (OPAC, PSA)	✓	✓	✓	✓
DLR (Cologne)	✓	N.A.	×	N.A.
Fraunhofer ISE	✓	✓	✓	✓
HUJI	✓	✓	×	✓
INTA	✓	✓	✓	✓
PROMES-CNRS	✓	✓	✓	✓
Number of participants	8	7	6	7

Table 7
Calibrated reference samples for baseline measurements.

Reference sample	Black coating		SSC	
Participant	*UV-VIS-NIR*	*Infrared*	*UV-VIS-NIR*	*Infrared*
Brightsource Industries	NIST traceable, diffuse sample	NIST traceable, specular gold coupon	NIST traceable, diffuse coupon	NIST traceable, specular gold coupon
CIEMAT (Madrid)	Labsphere calibrated, White diffuse	Gold diffuse	Labsphere calibrated, White diffuse	Gold diffuse
CIEMAT-DLR (OPAC, PSA)	OMT calibrated, Black sample	OMT calibrated, Black sample	OMT calibrated, Black sample	OMT calibrated, SSC sample
DLR (Cologne)	Black sample, OMT calibrated	N.A.	N.A.	N.A.
Fraunhofer ISE(*)	NIST traceable, white diffuse	NPL calibrated, sprayed aluminum	TNO calibrated, aluminium mirror	NPL calibrated, aluminum mirror
HUJI	White diffuse	Carbon or stainless steel	White diffuse	Carbon or stainless steel
INTA	Labsphere calibrated, White diffuse	AZ Technology, Gold diffuse	Labsphere calibrated, White diffuse	AZ Technology, Gold specular
PROMES-CNRS	Labsphere calibrated, White diffuse	AVIAN Technologies, Gold diffuse	Labsphere calibrated, White diffuse	NIST traceable, Gold specular

$$\alpha_{sol}(AM) = \frac{\int_{\lambda_1}^{\lambda_2} \left[1 - \rho_{sample,corr}(\lambda,\theta,T_{amb})\right].G_{sol}(\lambda,AM)d\lambda}{\int_{\lambda_1}^{\lambda_2} G_{sol}(\lambda.AM)d\lambda} \quad (4)$$

The thermal emittance ε_{th} is calculated for each reference sample, weighting the sample reflectance $\rho_{sample,corr}$ with a reference blackbody spectrum at a given absorber temperature T_{abs} according to (Eqs. (5) and (6)). The common integration interval is defined from $\lambda_1 = 0.3$ to $\lambda_3 = 16$ µm. For a given integration interval [λ_1 – λ_3], the fraction $f_{\sigma T^4}$ of Stefan Boltzmann law is expressed in (Eq. (7)).

Alternative upper limits are considered, i.e. 20, 25 and 50 µm, using spectral data up to 25 µm, if available, or extrapolating spectra otherwise, assuming reflectance is constant beyond 16 µm While ISO 22975–3:2014 [16] suggests that a constant value may be assumed beyond 25 µm, this is not always valid and this assumption depends on the coating [62-63].

$$\varepsilon_{th,calc}(T_{abs}) = \frac{\int_{\lambda_1}^{\lambda_3} \left[1 - \rho_{sample,corr}(\lambda,\theta,T_{amb})\right].E_{bb}(\lambda,T_{abs})d\lambda}{\int_{\lambda_1}^{\lambda_3} E_{bb}(\lambda,T_{abs})d\lambda} \quad (5)$$

$$E_{bb}(\lambda,T_{abs}) = \frac{2\pi hc^2}{\lambda^5\left[exp\left(\frac{hc}{\lambda kT_{abs}}\right) - 1\right]} \quad (6)$$

$$f_{\sigma T^4} = \frac{\int_{\lambda_1}^{\lambda_3} E_{bb}(\lambda,T_{abs})d\lambda}{\int_0^{\infty} E_{bb}(\lambda,T_{abs})d\lambda} = \frac{\int_{\lambda_1}^{\lambda_3} E_{bb}(\lambda,T_{abs})d\lambda}{\sigma T^4} \quad (7)$$

Reference solar spectra are plotted in Fig. 8 a from 0 to 4 µm, while the AM1.5 direct + circumsolar spectrum is compared against blackbody spectra at 25 °C and 750 °C from 0 to 50 µm in Fig. 8 b. Coverage fraction $f_{\sigma T^4}$ are shown as a function of blackbody temperature, respectively for benchtop spectrophotometers in Fig. 8 c and portable emissometers in Fig. 8 d.

As the blackbody temperature increases, the blackbody spectrum progressively overlaps with the solar spectrum in the UV-VIS-NIR range according to Wien's displacement law (Fig. 8b), justifying the concatenation of UV-VIS-NIR and Infrared spectral datasets. Adjusting the upper integration limit toward 50 µm allows achieving a higher coverage fraction at lower temperature (Fig. 8c). Portable emissometers show variable behavior in terms of coverage fraction (Fig. 8d). While the SOC device allows computing a ε_{th} value at a given absorber temperature, AZ Temp2000A only reports a value at ambient temperature 25°C, D&S AE1/RD1 reports a ε_{th} value at an intermediate temperature of 65°C, as its calorimetric measurement principle requires heating the sample on a heat sink plate.

2.4.3. Opto-thermal efficiency

Both standard figures of merit α_{sol} and ε_{th} can be combined into a compound figure of merit, namely the opto-thermal efficiency $\eta_{opt\text{-}th}$ [31, 37-38], which is expressed in (Eq. (8)). This equation assumes a flat plate geometry, negligible convection losses and a negligible heat sink temperature. Furthermore, the thermal emittance is supposedly calculated for a coverage fraction $f_{\sigma T^4} = 100\%$.

$$\eta_{opt-th} \approx \frac{\alpha_{sol}.\dot{q}''_{sol} - \varepsilon_{th}(T).\sigma T^4}{\dot{q}''_{sol}} = \alpha_{sol} - \frac{\sigma T^4}{\dot{q}''_{sol}}.\varepsilon_{th}(T) \quad (8)$$

Taking the partial derivative of $\eta_{opt\text{-}th}$ with respect to α_{sol} and ε_{th} (Eq. (9)), a trade-off factor Z can be defined between both figures of merit (Eq. (10)), which is a function of the operating conditions, i.e. absorber

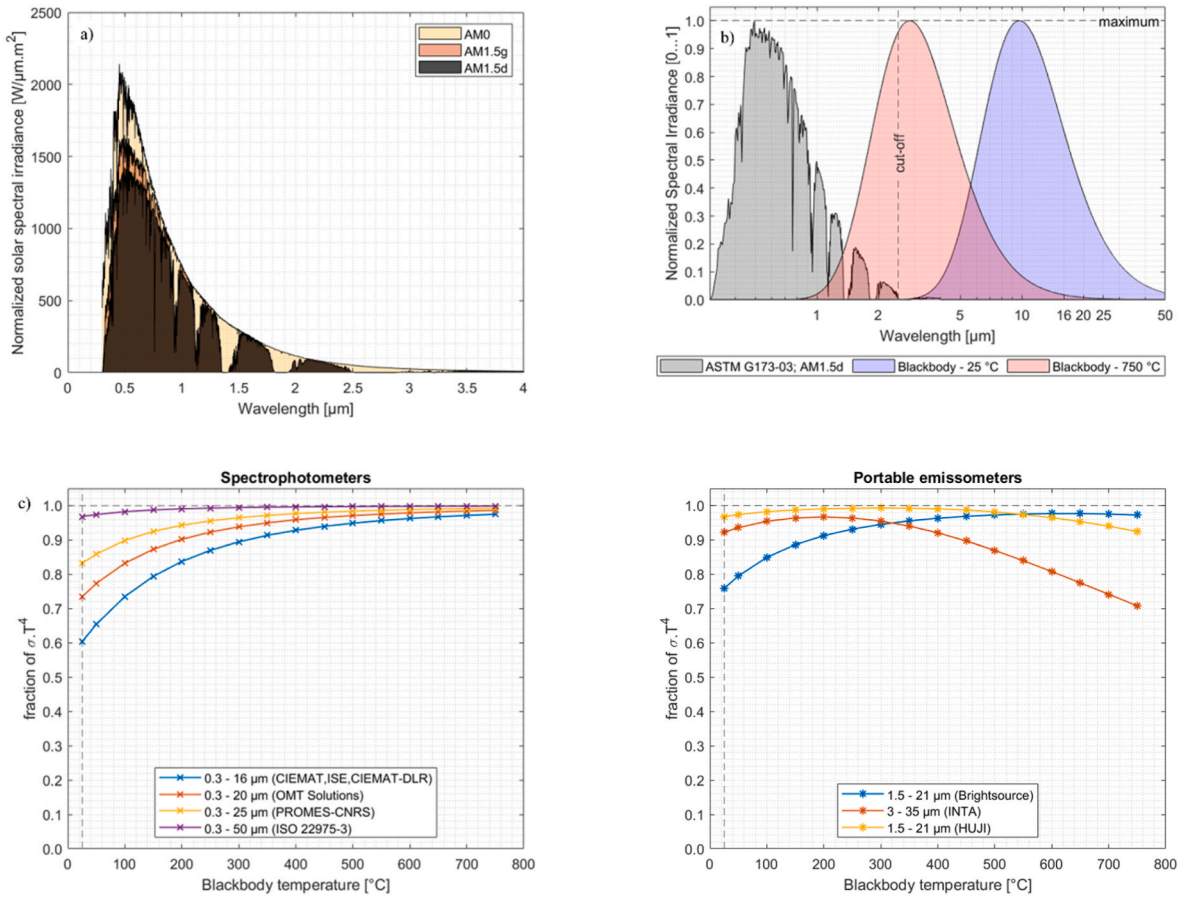

Fig. 8. Spectral weighting functions. a) ASTM G173-03 reference solar spectra. b) ASTM G173-03 Am1.5d and blackbody spectra a t 25 and 750 °C. c) Fraction of Stefan Boltzmann law (σT^4) as a function of blackbody temperature for benchtop spectrophotometers d) Fraction of σT^4 for portable emissometers.

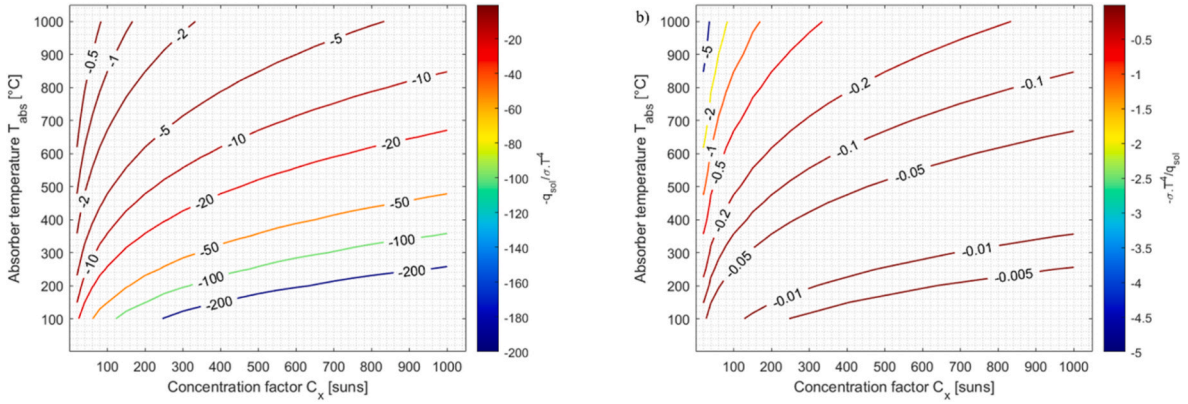

Fig. 9. Opto-thermal efficiency a) trade-off factor Z b) weighting coefficient for ε_{th} uncertainty.

temperature T and the concentrated solar flux q''_{sol}.

$$\frac{\partial \eta_{opt-th}}{\partial \alpha_{sol}} = 1; \quad \frac{\partial \eta_{opt-th}}{\partial \varepsilon_{th}} = -\frac{\sigma T^4}{q''_{sol}} \tag{9}$$

$$Z = \frac{\Delta \varepsilon_{th}}{\Delta \alpha_{sol}} = -\frac{q''_{sol}}{\sigma T^4} \tag{10}$$

The trade-off factor can be interpreted as follows: if α_{sol} is increased by +1 p.p., by how many percentage points does the ε_{th} value have to be reduced to achieve a constant $\eta_{opt\text{-}th}$?

Partial derivatives can also be used further to calculate the uncertainty propagation of α_{sol} and ε_{th} on the compound figure of merit $\eta_{opt\text{-}th}$, as expressed in (Eq.(11) and (12)).

$$u_c\left(\eta_{opt-th}\right)\Big|_{\{q''_{sol};T\}} = \sqrt{\left(\frac{\partial \eta_{opt-th}}{\partial \alpha_{sol}}.\Delta\alpha_{sol}\right)^2 + \left(\frac{\partial \eta_{opt-th}}{\partial \varepsilon_{th}}.\Delta\varepsilon_{th}\right)^2} \tag{11}$$

$$u_c\left(\eta_{opt-th}\right)\Big|_{\{q''_{sol};T\}} = \sqrt{\Delta\alpha_{sol}{}^2 + \left(-\frac{\sigma T^4}{q''_{sol}}.\Delta\varepsilon_{th}\right)^2} \tag{12}$$

The trade-off factor Z is shown in Fig. 9 a. as a function of the operating point, i.e. the absorber temperature and the concentration ratio $\{T_{abs}; C_x\}$, while the weighting coefficient of the thermal emittance error, i.e. 1/Z, is shown in Fig. 9 b. Thermal emittance is important at a

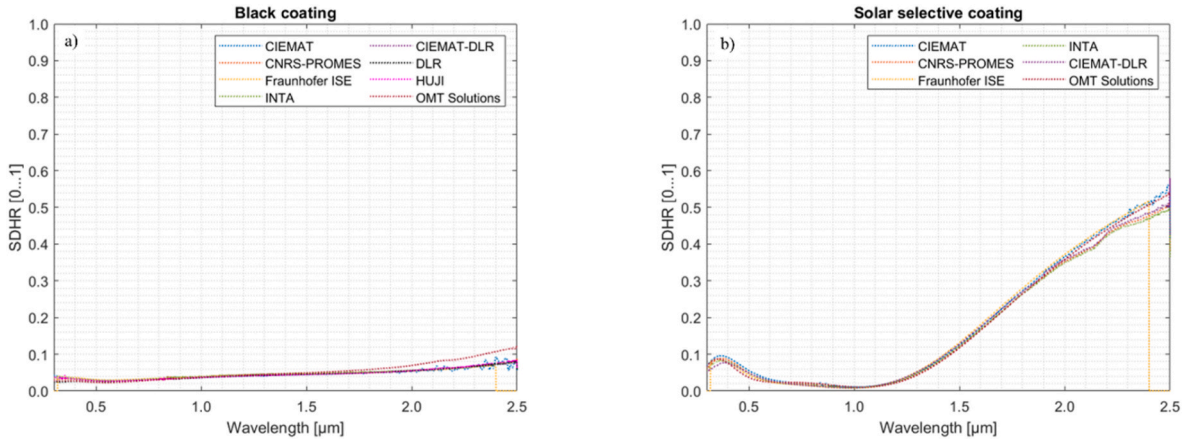

Fig. 10. UV-VIS-NIR spectral datasets. a) Black coating, b) Solar selective coating.

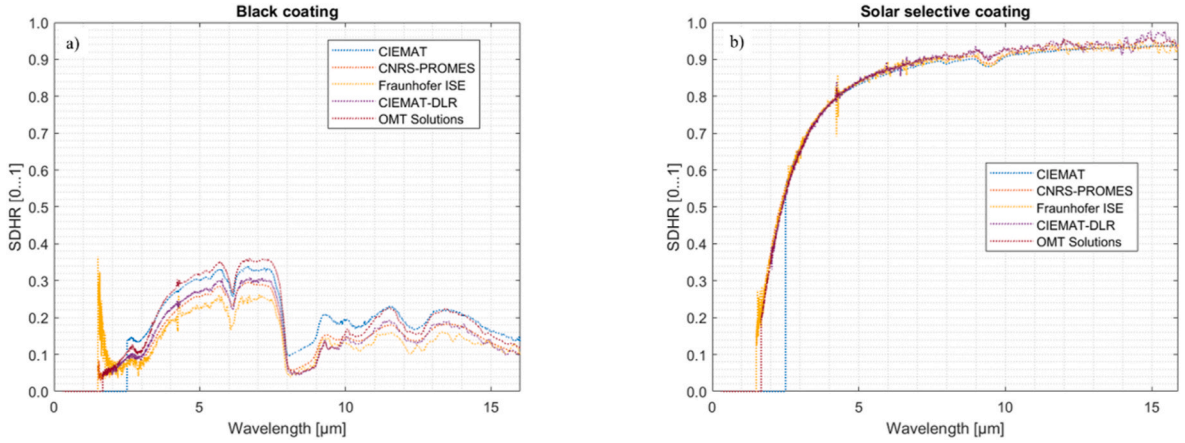

Fig. 11. Infrared spectral datasets. a) Black coating, b) Solar selective coating.

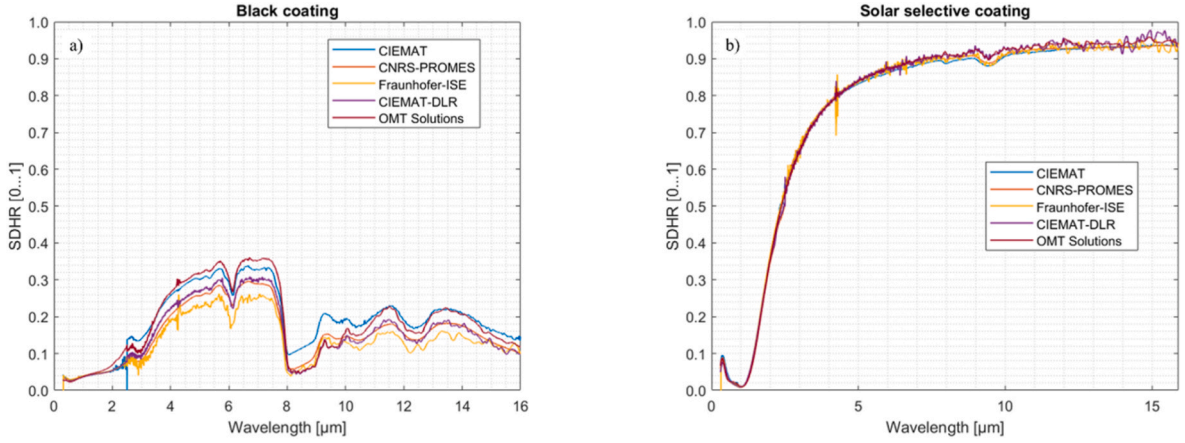

Fig. 12. Concatenated spectral datasets from 0.3 to 16 μm. a) Black coating, b) Solar selective coating.

low concentration ratio and a high absorber temperature (top left corner), while solar absorptance is dominant at a high concentration ratio and a low absorber temperature (bottom right corner). For example, at $C_x \sim 20$ suns and $T_{abs} \sim 300$ °C (parabolic trough), increasing α_{sol} by +1 p.p. has the same effect on $\eta_{opt\text{-}th}$ as reducing ε_{th} by Z ~ -3.3 p.p, thus favoring solar selective coatings. At $C_x \sim 1000$ suns and $T_{abs} \sim 300$ °C (central receiver system), the value of the trade-off factor Z is ~ -163 p.p, in this case high solar absorptance black coatings become more relevant.

3. Results and discussion

3.1. Spectral processing

Spectral datasets obtained from benchtop spectrophotometers for black and SSC samples are respectively plotted over the UV-VIS-NIR

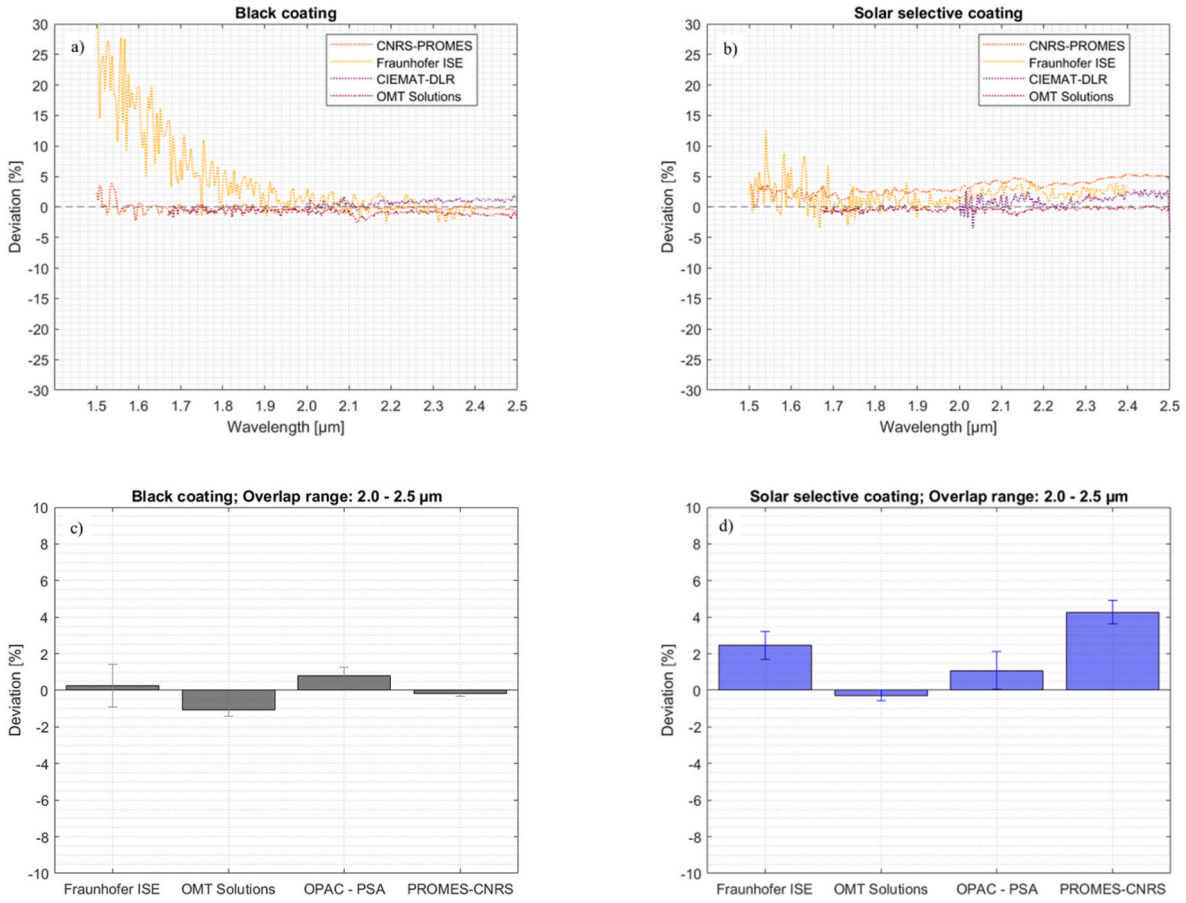

Fig. 13. Spectral deviation between UV-VIS-NIR and infrared spectrophotometers. a) Spectral deviation, black coating b) Spectral deviation, solar selective coating. c) Average mismatch (2 – 2.5 µm), black coating. d) Average mismatch (2 – 2.5 µm), solar selective coating.

Table 8
Spectral mismatch statistics.

	Black coating		Solar selective coating	
Participant	*mean [%]*	*stdev [%]*	*mean [%]*	*stdev [%]*
CIEMAT-DLR (OPAC, PSA)	0.8%	0.5%	1.1%	1.1%
Fraunhofer ISE	0.3%	1.2%	2.5%	0.7%
PROMES-CNRS	−0.2%	0.2%	4.3%	0.6%
OMT Solutions	−1.1%	0.4%	−0.3%	0.3%

spectral range in Fig. 10 and over the infrared range in Fig. 11. In the UV-VIS-NIR range, spectral datasets are consistent among participant up to 2 µm. In the infrared range, a dispersion of a few percentage points can be observed for the black coating, while a consistent spectral behavior is observed for the SSC up to 16 µm. For CIEMAT-DLR dataset, the low detector sensitivity above 16 µm induces an important waviness. A spike can be observed around 4.3 µm in some datasets, as CO_2 atmospheric absorption is not corrected by nitrogen purging during spectral measurements.

Concatenated spectral datasets from 0.3 to 16 µm are shown in Fig. 12. Spectral datasets from 0.3 to 2.5 µm are taken from UV-VIS-NIR measurements (Fig. 10), while datasets above 2.5 µm are taken from FTIR measurements (Fig. 11). The spectral mismatch in the overlap range between UV-VIS-NIR and infrared spectrophotometers is analyzed in Fig. 13, including mismatch statistics computed over the common overlapping spectral range from 2 to 2.5 µm, according to (Eq. (3)). Detailed mismatch statistics is listed in Table 8 for this spectral range.

It is worth observing on Fig. 12 that spectral datasets agree reasonably well, considering the experimental uncertainty of acquired reflectance spectra. The experimental uncertainty of the PerkinElmer Lambda 1050 has been analyzed in details for specular mirrors in Ref. [64] and a maximum combined standard uncertainty $u_c = 0.008$ (k = 1) has been reported. For FTIR measurements, OMT Solutions communicates a combined standard uncertainty $u_c = 0.01$ (k = 2) for accurate measurements on flat diffuse gold samples. For UV-VIS-NIS measurements, spectral datasets agree within ±1.p.p. for black and selective samples, up to ~ 2 µm. For FTIR measurements, spectral datasets agree within ±2 p,p. for selective samples, while a standard deviation of ~± 3 p,p. is observed for black samples beyond 2 µm, affecting further spectral weighting.

The spectral mismatch characterizes the deviation between UV-VIS-NIR and FTIR spectrophotometers in a common spectral range. A significant spectral deviation is observed from 1.5 to 2 µm for the black coating in Fraunhofer ISE dataset. This spectral range is discarded from the statistical analysis. The average spectral mismatch (2–2.5 µm) lies respectively between -1.1% and 0.8% for the black coating and between -0.3% and 4.3% for the SSC. Spectral mismatch is seldom described in the literature. However, it is a valuable quality indicator for the optical measurement process and baseline selection. A minimal value should be ideally achieved. Nonetheless, noisy detector signals, reference sample choices and integrating sphere configurations are mainly responsible for this mismatch.

3.2. *Spectral weighting*

Calculated α_{sol} values according to ASTM G173-03 are shown in Fig. 14 and reported in Table 9. At AM1.5d, the black coating has a mean α_{sol} value of 96.6% and a standard deviation of 0.16%, while the SSC a mean α_{sol} value of 94.5% and a standard deviation of 0.35%. A higher

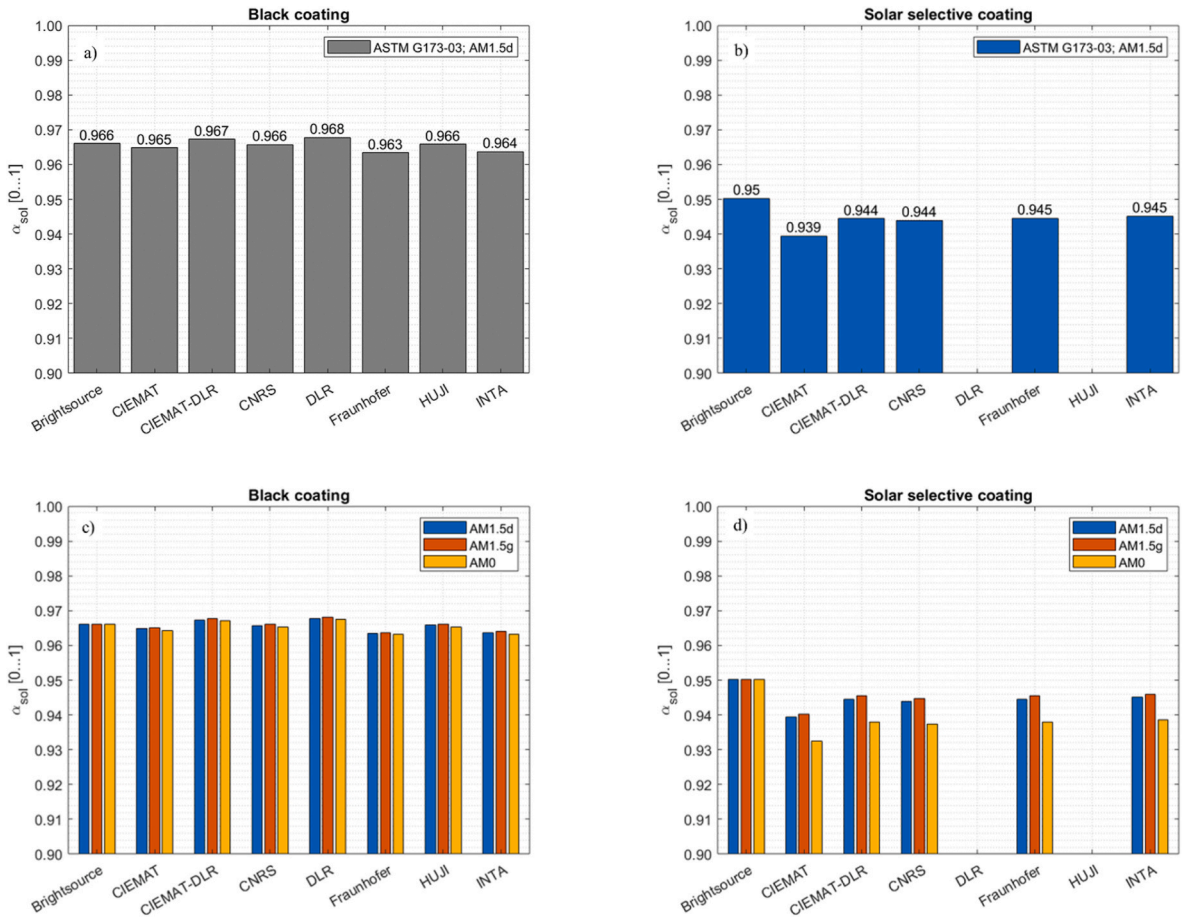

Fig. 14. Solar absorptance calculations according to ASTM G173-03 a) Black coating, direct + circumsolar, b) Solar selective coating, direct + circumsolar, c) Black coating, AM0/AM1.5g/AM1.5d d) Solar selective coating, AM0/AM1.5g/AM1.5d.

Table 9
Solar absorptance calculations according to ASTM G173-03.

Measurand	α_{sol} (ASTM G173-03) [%]					
Sample	*Black coating*			*Solar selective coating*		
Participant	*AM0*	*AM1.5g*	*AM1.5d*	*AM0*	*AM1.5g*	*AM1.5d*
Brightsource Industries	–	96.6%	–	–	95.0%	–
CIEMAT (Madrid)	96.42%	96.50%	96.48%	93.24%	94.00%	93.93%
CIEMAT-DLR (OPAC, PSA)	96.71%	96.77%	96.73%	93.81%	94.53%	94.43%
DLR (Cologne)	96.76%	96.82%	96.78%	–	–	–
Fraunhofer ISE	96.32%	96.36%	96.34%	93.79%	94.54%	94.44%
HUJI	96.53%	96.61%	96.58%	–	–	–
INTA	96.33%	96.40%	96.37%	93.86%	94.58%	94.50%
PROMES-CNRS	96.53%	96.60%	96.57%	93.73%	94.45%	94.38%
Mean value	**96.53%**	**96.58%**	**96.56%**	**93.91%**	**94.52%**	**94.45%**
Standard deviation	**0.16%**	**0.16%**	**0.16%**	**0.59%**	**0.33%**	**0.35%**

deviation is thus observed for the SSC. A higher sensitivity to the solar spectrum is also observed for the SSC (Spread AM0 vs. AM1.5d: 0.5%) than for the black coating (Spread AM0 vs. AM1.5d: 0.03%).

Calculated ε_{th} values are shown in Fig. 15 and reported in Table 10. Values are reported over the temperature range from 25 to 750 °C. Consistent curves are calculated for the SSC, while a deviation of a few percentage points is observed for the black coating, in line with spectral deviations observed in Fig. 11 a. At 650 °C, the standard deviation on ε_{th} is respectively 3.8% for the black coating and 0.5% for the SSC.

Values reported by portable devices are also displayed on Fig. 15 a and Fig. 15 b. Although a direct comparison is not feasible, due to different spectral ranges and reference temperatures, values obtained with the TEMP2000A at 25°C are in line with thermal emittance curves for both samples. The SOC ET-100 portable emissometer computes an accurate value at 650 °C for the SSC, while the value reported for the black coating is lower than the mean value by a few percentage points. Finally, the D&S AE1/RD1 emissometer reports a correct value for the black coating, but the value reported for the SSC lies significantly above the mean ε_{th} value.

The D&S AE1/RD1 device has a lower resolution, as values are reported without any decimal unit, with a reported uncertainty of ±1.4 p. p.Meanwhile, the TEMP2000 A portable device reports values with one decimal unit, with an uncertainty of ±1 p.p. for gray samples and ±3 p. p. for non gray samples according to the device manual [55]. For the

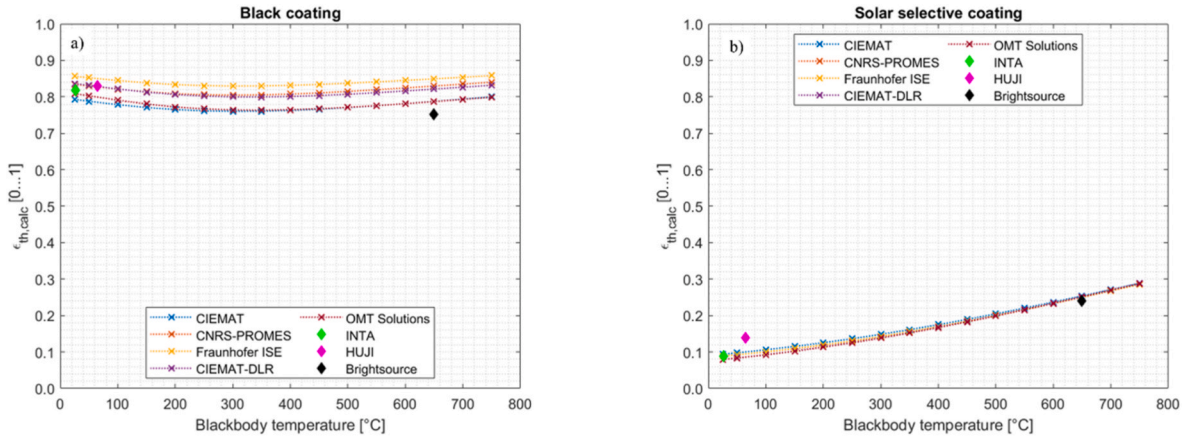

Fig. 15. Thermal emittance calculations. For benchtop spectrophotometers, the integration interval spans here from 0.3 to 16 μm. a) Black coating b) Solar selective coating.

Table 10
Thermal emittance calculations. Integration interval for spectrophotometers: from 0.3 to 16 μm. (*) The outlying value reported for the SSC by the D&S AE1/RD1 is omitted in the standard deviation calculation.

Measurand		$\varepsilon_{th,calc}$ (T)			
Sample	*Spectral range*	*Black coating*		*SSC*	
Participant	[μm]	*25 °C*	*650 °C*	*25 °C*	*650 °C*
Brightsource Industries (*)	[1.5 21]	N.A.	75.2%	N.A.	24.0%
CIEMAT (Madrid)	[0.3–16]	79.3%	78.7%	9.39%	25.4%
CIEMAT-DLR (OPAC, PSA)	[0.3–16]	83.6%	82.1%	7.96%	25.2%
Fraunhofer ISE	[0.32–16]	85.6%	84.9%	8.88%	25.0%
HUJI (* 65°C)	[2–50]	83%	N.A.	14%	N.A.
INTA	[3–35]	81.9%	N.A.	8.76%	N.A.
PROMES-CNRS	[0.3–16]	83.4%	83.0%	8.90%	25.1%
Mean value		**82.8%**	**80.8%**	**9.7%**	**25.0%**
Standard deviation		**2.1%**	**3.8%**	**0.5% (*)**	**0.5%**

SOC portable device, the reflectance accuracy for the 20° incidence angle reported by the manufacturer [52–54] is ±3 p.p. for any spectral band, i.e. for the 410-Solar and the ET-100 measurement heads.

The wavelength interval upper limit is extended from 16 μm toward 50 μm for ε_{th} calculations with benchtop spectrophotometers. Deviations with respect to 16 μm are shown in Fig. 16. For the black coating, calculated ε_{th} values increase by a few percentage points at lower temperature as the upper limit shifts toward 50 μm, as the fraction $f_{\sigma T^4}$ increases (Fig. 8c). The opposite trend is observed for the SSC, i.e. calculated ε_{th} values decrease for similar conditions.

At higher temperatures, calculated values converge while the dispersion decreases, regardless of the upper integration limit for the black coating. As the blackbody spectral irradiance shifts to shorter wavelengths according to Wien's displacement law, the far infrared spectrum has a lower influence in the calculation. For the solar selective coating, a systematic offset, lower than one percentage point, remains at higher temperature. Shifting the upper wavelength limit gives more weight to the high reflectance asymptote in the calculation (Fig. 7). Nonetheless, assuming a constant reflectance level beyond 16 μm, following the ISO 22975-3 as a guideline [16], may not be an appropriate rule for a SSC, as shown in the literature [62,63]. A sigmoid spectral model [15] may be a better alternative to estimate the asymptotical behavior and smooth far infrared spectral measurement noise.

3.3. Opto-thermal efficiency

The opto-thermal efficiency $\eta_{opt\text{-}th}$ is calculated for a set of operating points $\{T_{abs}; C_x\}$ according to (Eq. (8)), using α_{sol} and temperature dependent ε_{th} values derived in Section 3.2. Contour maps are shown for both coatings in Fig. 17. The $\eta_{opt\text{-}th}$ value converges towards α_{sol} at low temperature, as the thermal emission becomes negligible. The black coating outperforms the solar selective coating at low temperature and high concentration (bottom right corner), while the solar selective coating performs better than the black coating at higher temperature and low concentration (top left corner). A Pareto front exists where both coatings have a similar opto-thermal efficiency [15].

The propagation of measurement uncertainties on $\eta_{opt\text{-}th}$ is calculated according to (Eq. (12)), estimating the respective uncertainties on $\Delta\alpha_{sol}$ and $\Delta\varepsilon_{th}$ from Section 3.2, neglecting any temperature dependence. Results are shown for both coatings in Fig. 18. The uncertainty term $\Delta\alpha_{sol}$ is dominant, according to Fig. 9. It corresponds to the lower uncertainty bound $u_c(\eta_{opt\text{-}th})$. On the other hand, the uncertainty term $\Delta\varepsilon_{th}$ gains weight at higher temperature and becomes dominant for low concentration factor ($C_x < 10$).

4. Conclusion

In this study, spectral directional hemispherical reflectance measurements have been compared at several laboratories on two flat solar thermal absorber coatings, i.e. a high absorbing black coating and a solar selective coating. Measurements have been carried out at room temperature both with benchtop spectrophotometers and portable devices.

A good agreement was found between spectrophotometer datasets. In the UV-VIS-NIR range, all datasets agree well until 2.0 μm. Above 2.5 μm, a minor deviation can be observed for both coatings. In the Infrared range, a good agreement is observed for the solar selective coating until 16 μm. For the black coating, a higher dispersion is noticeable. Spectral mismatch in the range from 2 to 2.5 μm is less than 1 p.p. for the black coating, while a slightly higher deviation is noticed for the SSC.

Applying ASTM G173-03 (direct + circumsolar), the α_{sol} average and standard deviation are respectively 96.6 ± 0.16% for the black coating and 94.5 ± 0.35% for the SSC. The selection of the reference solar spectrum does not significantly affect the α_{sol} calculation for the black coating, while the sensitivity is more pronounced for the solar selective coating. The SOC 410-Solar portable device delivers values in agreement with benchtop spectrophotometers. .

For ε_{th} calculations, a good agreement is found for the SSC (650 °C: $\varepsilon_{th,calc} = 25.0 \pm 0.5\%$), while a larger deviation can be noticed for the black coating (650 °C: $\varepsilon_{th,calc} = 80.8 \pm 3.8\%$), mainly explained by the

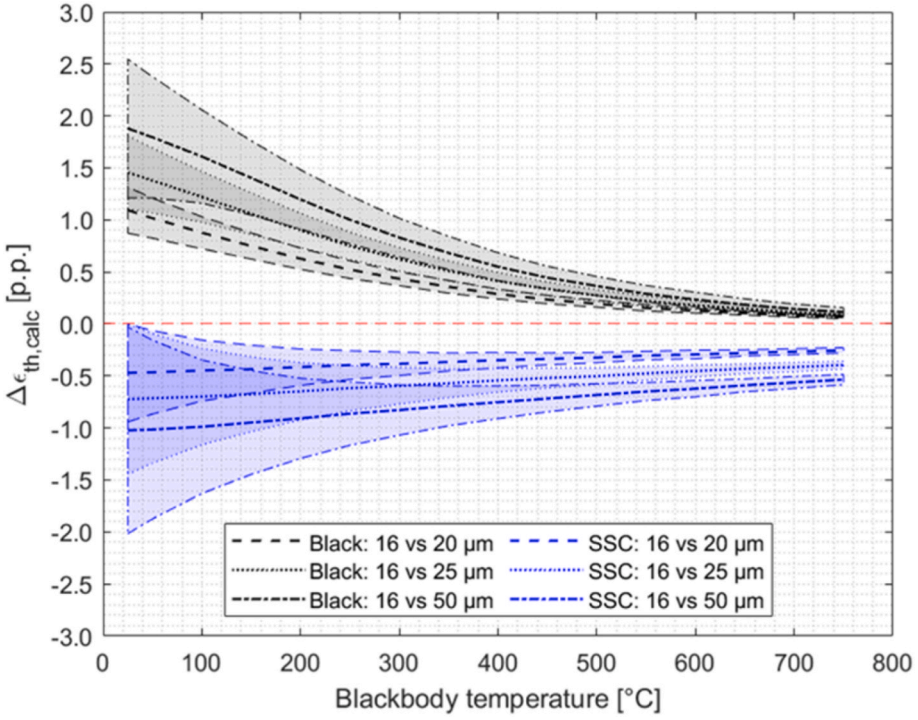

Fig. 16. Deviation in ε_{th} calculations after adjusting the integration interval from 16 µm toward 50 µm.

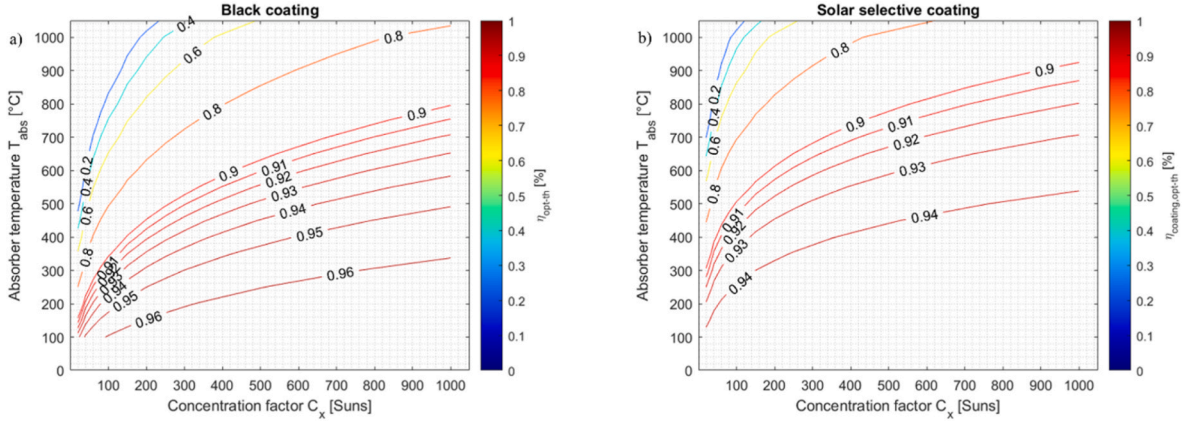

Fig. 17. Opto-thermal efficiency a) Black coating b) Solar selective coating.

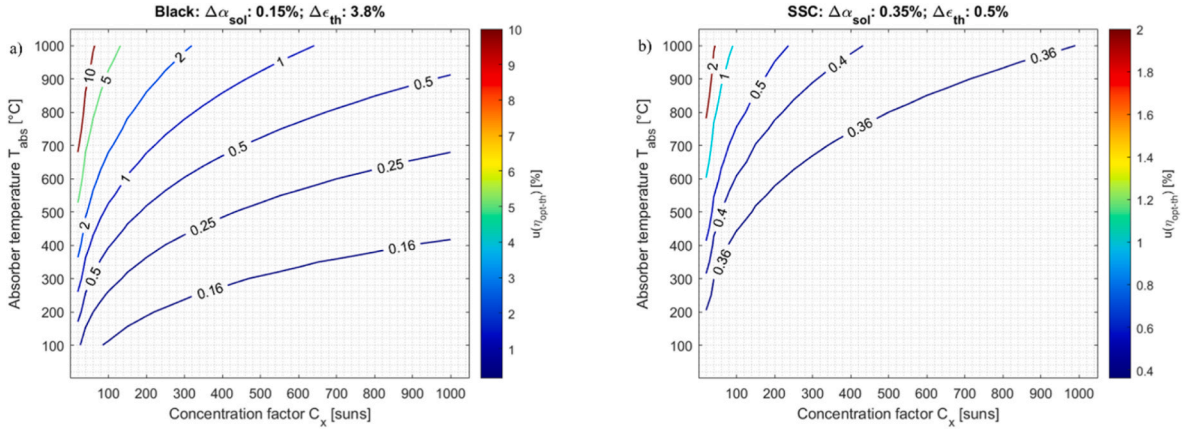

Fig. 18. Propagation of uncertainty on the opto-thermal efficiency.

dispersion of infrared spectra. The calculated temperature dependence of ε_{th} is moderate for the black coating and more pronounced for the solar selective coating, as the overlap of the blackbody and solar spectra increases.

Extrapolating spectral data from 16 to 50 μm has a moderate impact on ε_{th} calculation results. For the black coating, ε_{th} values converge at higher temperature, while their dispersion decreases. For the solar selective coating, a systematic offset of 1 p.p. remains at higher temperature, as more weight is given to the solar selective coating high reflectance at long wavelengths. Extrapolating spectral data beyond 16 μm according to ISO 22975–3 may not be a suitable guideline for any coating. In the case of solar selective coating, sigmoid models or far infrared measurements provide a more realistic asymptotical reflectance value.

The comparison of portable emissometers show that the AZ Technology Temp 2000A device agrees best with benchtop spectrophotometers. It reports however a single value at 300 K, while the SOC ET-100 can perform calculations over a broader temperature range, thanks to its multispectral configuration.

The analysis of the coating opto-thermal efficiency $\eta_{opt\text{-}th}$ shows that the black coating and solar selective coating optimal operating ranges are complementary. The propagation of α_{sol} and ε_{th} uncertainties on the opto-thermal efficiency $\eta_{opt\text{-}th}$ were further analyzed. At low temperature and high concentration factor, the α_{sol} parameter is dominant and its uncertainty defines the lower bound for the combined uncertainty u_c ($\eta_{opt\text{-}th}$), while ε_{th} parameter is more dominant at high temperature and low concentration factor and its accuracy gradually affects the combined uncertainty u_c ($\eta_{opt\text{-}th}$).

CRediT authorship contribution statement

Simon Caron: Conceptualization, Investigation, Software, Methodology, Visualization, Validation, Writing – original draft, Writing – review & editing. **Leslie Herding:** Conceptualization, Writing – review & editing, Writing – original draft, Visualization, Validation, Software, Methodology. **Yaniv Binyamin:** Investigation, Resources, Writing – review & editing. **Mubeen Baidossi:** Writing – review & editing, Investigation, Resources. **Yelena Vinetsky:** Investigation, Resources, Writing – review & editing. **Angel Morales:** Writing – review & editing, Resources, Investigation. **Christina Hildebrandt:** Investigation, Resources, Writing – review & editing. **Reine Reoyo-Prats:** Writing – review & editing, Resources, Investigation. **Olivier Faugeroux:** Investigation, Resources, Writing – review & editing. **Alina Agüero:** Investigation, Writing – review & editing, Resources. **Sergio Rodriguez:** Writing – review & editing, Resources, Investigation. **Florian Sutter:** Funding acquisition, Project administration, Writing – review & editing. **Marc Röger:** Writing – review & editing, Supervision, Methodology. **Francisco Manzano-Agugliaro:** Supervision, Visualization, Writing – review & editing.

Declaration of competing interest

The authors declare that they have no known competing financial interests or personal relationships that could have appeared to influence the work reported in this paper.

Acknowledgments

Financial support from the European Union is gratefully acknowledged (EU-Raiselife project, Horizon 2020, Contract n° 686008). The author thanks the OPAC laboratory technical staff: Lucia Martinez, Carmen Amador and Tomas Reche for their technical assistance in optical measurements. This project (EU SFERA-III) has received funding from the European Union's Horizon 2020 Research and Innovation Program under grant agreement n○ 823802

References

[1] K. Lovegrove, J. Pye, Concentrating Solar Power Technology: Principles, Developments and Applications, second ed., Woodhead Publishing, 2020 https://doi.org/10.1016/C2018-0-04978-6.
[2] World Bank, Concentrating solar power: clean power on demand 24/7, 65, https://pubdocs.worldbank.org/en/849341611761898393/WorldBank-CSP-Report-Concentrating-Solar-Power-Clean-Power-on-Demand-24-7-FINAL.pdf, 2021. (Accessed 28 July 2021).
[3] German Aerospace Center (DLR) Institute of Solar Research, Solar thermal power plants: heat, electricity and fuels from concentrated solar power, 27, https://www.dlr.de/sf/en/PortalData/73/Resources/dokumente/publikationen_medien/dlr_und_sf/Study_Solar_thermal_power_plants_DLR_2021-05.pdf, 2021. (Accessed 28 July 2021).
[4] J. Lilliestam, R. Pitz-Paal, Concentrating solar power for less than USD 0.07 per kWh : finally the breakthrough, Renewable Energy Focus 26 (2018) 17–21, https://doi.org/10.1016/j.ref.2018.06.002.
[5] A. Fernandez-Garcia, E. Zarza, L. Valenzuela, M. Perez, Parabolic-trough solar collectors and their applications, Renew. Sustain. Energy Rev. 14 (7) (2010) 1695–1721, https://doi.org/10.1016/j.rser.2010.03.012.
[6] J. Frederiksson, M. Eickhoff, L. Giese, M. Herzog, A comparison and evaluation of innovative parabolic trough collector concepts for large-scale application, Sol. Energy 215 (2021) 266–310, https://doi.org/10.1016/j.solener.2020.12.017.
[7] C.K. Ho, B.D. Iverson, Review of high-temperature central receiver designs for concentrated solar power, Renew. Sustain. Energy Rev. 29 (2014) 835–846, https://doi.org/10.1016/j.rser.2013.08.099.
[8] C.K. Ho, Advances in central receivers for concentrating solar applications, Sol. Energy 152 (2017) 38–56, https://doi.org/10.1016/j.solener.2017.03.048.
[9] G. Zhu, T. Wendelin, M.J. Wagner, C. Kutscher, History, Current State, and future of linear Fresnel concentrating solar collectors, Sol. Energy 103 (2014) 69–652, https://doi.org/10.1016/j.solener.2013.05.021.
[10] J. Coventry, C. Andraka, Dish systems for CSP, Sol. Energy 152 (2017) 140–170, https://doi.org/10.1016/j.solener.2017.02.056.
[11] A. Bonk, S. Sau, M. Uranga, M. Hernaiz, T. Bauer, Advanced heat transfer fluids for direct molten salt line-focusing CSP plants, Prog. Energy Combust. Sci. 67 (2018) 69–87, https://doi.org/10.1016/j.pecs.2018.02.002.
[12] A. Bonk, M. Braun, V.A. Sötz, T. Bauer, Solar Salt – pushing an old material for energy storage to a new limit, Appl. Energy 262 (15) (2020) 7, https://doi.org/10.1016/j.apenergy.2020.114535, 114535.
[13] L.L. Vant-Hull, The role of "allowable flux density" in the design and operation of molten-salt solar central receivers, J. Sol. Energy Eng. 124 (2) (2002) 165–169, https://doi.org/10.1115/1.1464124.
[14] Z. Liao, X. Li, C. Xu, C. Chang, Z. Wang, Allowable flux density on a solar central receiver, Renew. Energy 62 (2014) 747–753, https://doi.org/10.1016/j.renene.2013.08.044.
[15] S. Caron, J. Garrido, J. Ballestrin, F. Sutter, M. Röger, F. Manzano-Agugliaro, A comparative analysis of opto-thermal figures of merit for high temperature solar thermal absorber coatings, Renew. Sustain. Energy Rev. 154 (2022) 21, https://doi.org/10.1016/j.rser.2021.111818, 111818.
[16] International Organization for Standardization, Solar Energy – Collector Components and Materials – Part3: Absorber Surface Durability, ISO 22975-3: 2014, 2014, p. 30, 28/07/21, https://www.iso.org/standard/61758.html.
[17] International Organization for Standardization, Space Systems – Measurement of Thermo-Optical Properties of Thermal Control Materials, ISO 16378:2013, 2013, p. 36, 28/07/21, https://www.iso.org/standard/56558.html.
[18] ASTM International, Standard Test Method for Solar Absorptance, Reflectance, and Transmittance of Materials Using Integrating Spheres, ASTM E903:2020, 2020, p. 17, https://doi.org/10.1520/E0903-20.
[19] ASTM International, Standard Test Method for Determination of Solar Reflectance Near Ambient Temperature Using a Portable Solar Reflectometer, ASTM C1549: 2016, 2016, p. 6, https://doi.org/10.1520/C1549-16.
[20] ASTM International, Standard Test Method for Determination of Emittance of Materials Near Room Temperature Using Portable Emissometers, ASTM C1371: 2015, 2015, p. 8, https://doi.org/10.1520/C1371-15.
[21] ASTM International, Standard Test Methods for Total Normal Emittance of Surfaces Using Inspection-Meter Techniques, ASTM E408:2013, 2019, p. 5, https://doi.org/10.1520/E0408-13R19.
[22] ASTM International, Standard Test Method for Normal Spectral Emittance at Elevated Temperatures, ASTM E307:1972, 2019, p. 6, https://doi.org/10.1520/E0307-72R19.
[23] ASTM International, Standard Test Method for Total Hemispherical Emittance of Surfaces up to 1400°C, ASTM C835:2006, 2020, p. 11, https://doi.org/10.1520/C0835-06R20.
[24] L. Noč, E. Šest, G. Kapun, F. Ruiz-Zepeda, Y. Binyamin, F. Merzel, I. Jerman, High-solar-absorptance CSP coating characterization and reliability testing with isothermal cyclic loads for service-life prediction, Energy Environ. Sci. 12 (2019) 1679–1694, https://doi.org/10.1039/C8EE03536A.
[25] K. Tsuda, Y. Murakami, J.F. Torres, J. Coventry, Development of high absorption, high durability coatings for solar receivers in CSP plants, AIP Conf. Proc. (2018) 8, https://doi.org/10.1063/1.5067075, 2033: 040039.
[26] R. Harzallah, M. Larnicol, C. Leclercq, A. Herbein, F. Campana, Development of high performances solar absorber coatings, AIP Conf. Proc. (2019) 11, https://doi.org/10.1063/1.5117538, 2126:030026.
[27] I. Jerman, F.R. Zepeda, F. Merzel, L. Noč, High-temperature "ion baseball" for enhancing concentrated solar power efficiency, Sol. Energy Mater. Sol. Cell. 200 (2019) 12, https://doi.org/10.1016/j.solmat.2019.109974, 109974.

[28] F. Cao, K. McEnaney, G. Chen, Z. Ren, A review of cermet-based spectrally selective solar absorbers, Energy Environ. Sci. 7 (2014) 1615–1627, https://doi.org/10.1039/C3EE43825B.
[29] K. Xu, M. Du, L. Hao, J. Mi, Q. Yu, S. Li, A review of high-temperature selective absorber coatings for solar thermal applications, Journal of Materiomics 6 (1) (2020) 167–182, https://doi.org/10.1016/j.jmat.2019.12.012.
[30] C. Hildebrandt, High-temperature Stable Absorber Coatings for Linear Concentrating Solar Thermal Power Plants, PhD thesis, Stuttgart University, 2009, https://doi.org/10.18419/opus-1802.
[31] I. Heras Pérez, Multilayer Solar Selective Coatings for High Temperature Solar Applications: from Concept to Design, PhD thesis, Sevilla University, 2016, http://hdl.handle.net/11441/47789.
[32] C.K. Ho, A.R. Mahoney, A. Ambrosini, M. Bencomo, A. Hall, T.N. Lambert, Characterization of pyromark 2500 paint for high-temperature solar receivers, J. Sol. Energy Eng. 136 (1) (2014) 4, https://doi.org/10.1115/1.4024031, 014502.
[33] K. Burlafinger, A. Vetter, C.J. Barbec, Maximizing concentrated solar power (CSP) plant overall efficiencies by using spectral selective absorbers at optimal operation temperatures, Sol. Energy 120 (2015) 428–438, https://doi.org/10.1016/j.solener.2015.07.023.
[34] J. Coventry, P. Burge, Optical properties of Pyromark 2500 coatings of variable thicknesses on a range of materials for concentrating solar thermal applications, AIP Conf. Proc. (2017) 8, https://doi.org/10.1063/1.4984355, 1850: 030012.
[35] A. Ambrosini, A. Boubault, C.K. Ho, L. Banh, J.R. Lewis, Influence of application parameters on stability of Pyromark® 2500 receiver coatings, AIP Conf. Proc. (2019) 8, https://doi.org/10.1063/1.5117514, 2126:030002.
[36] S. Caron, J. Garrido, E. Setien, R. Harzallah, L. Noč, I. Jerman, M. Röger, F. Sutter, Forty shades of black: a benchmark of high temperature sprayable black coatings applied on Haynes 230, AIP Conf. Proc. (2020) 10, https://doi.org/10.1063/5.0028773, 2303:1560007.
[37] K. Zhang, L. Hao, M. Du, J. Mi, J.N. Wang, J.P. Meng, A review on thermal stability and high temperature induced ageing mechanisms of solar absorber coatings, Renew. Sustain. Energy Rev. 67 (2017) 1282–1299, https://doi.org/10.1016/j.rser.2016.09.083.
[38] A. Boubault, C.K. Ho, A. Hall, T.N. Lambert, A. Ambrosini, Durability of solar absorber coatings and their cost-effectiveness, Sol. Energy Mater. Sol. Cell. 166 (2017) 176–184, https://doi.org/10.1016/j.solmat.2017.03.010.
[39] C.K. Ho, J.E. Pacheco, Levelized Cost of Coating (LCOC) for selective absorber materials, Sol. Energy 108 (2014) 315–321, https://doi.org/10.1016/j.solener.2014.05.017.
[40] A. Boubault, C.K. Ho, A. Hall, T.N. Lambert, A. Ambrosini, Levelized cost of energy (LCOE) metric to characterize solar absorber coatings for the CSP industry, Renew. Energy 85 (2016) 472–483, https://doi.org/10.1016/j.renene.2015.06.059.
[41] Raiselife, EU project, Horizon (2020). http://www.raiselife.eu/. (Accessed 28 July 2021).
[42] S. Caron, F. Sutter, N. Algner, M. Esteller, Y. Binyamin, M. Baidossi, A. Kenigsberg, A. Agüero, D. Fähsing, C. Hildebrandt, Accelerated ageing of solar receiver coatings: experimental results for T91 and VM12 steel substrates, AIP Conf. Proc. 2033 (10) (2018) 230002, https://doi.org/10.1063/1.5067230.
[43] S. Caron, Y. Binyamin, M. Baidossi, A. Kenigsberg, A. Agüero, C. Hildebrandt, M. Galetz, F. Sutter, Durability testing of solar receiver coatings: experimental results for T91 and VM12 steel substrates, AIP Conf. Proc. (2018) 10, https://doi.org/10.1063/1.5067230, 2033:230002.
[44] R. Reoyo-Prats, A. Carling Plaza, O. Faugeroux, B. Claudet, A. Soum-Glaude, C. Hildebrandt, Y. Binyamin, A. Agüero, T. Meißner, Accelerated aging of absorber coatings for CSP receivers under real high solar flux – evolution of their optical properties, 193:92-100, https://doi.org/10.1016/j.solmat.2018.12.030, 2019.
[45] L. del Campo, R.B. Perez-Saez, X. Esquisabel, I. Fernandez, M.J. Tello, New experimental device for infrared spectral directional emissivity measurements in a controlled environment, Rev. Sci. Instrum. 77 (2006) 8, https://doi.org/10.1063/1.2393157, 113111.
[46] P. Honnerova, J. Martan, M. Kučera, M. Honner, J. Hameury, New experimental device for high-temperature normal spectral emissivity measurement of coatings, Meas. Sci. Technol. 25 (9) (2014) 9, https://doi.org/10.1088/0957-0233/25/9/095501, 095501.
[47] I. Setien-Fernandez, T. Echaniz, L. Gonzalez-Fernandez, R.B. Perez-Saez, E. Cespedes, J.A. Sanchez-Garcia, L. Alvarez-Fraga, R. Escobar Galindo, J. M. Albella, C. Prieto, M.J. Tello, First spectral emissivity study of a solar selective coating in the 150-600 °C temperature range, Sol. Energy Mater. Sol. Cell. 117 (2013) 390–395, https://doi.org/10.1016/j.solmat.2013.07.002.
[48] T. Echaniz, I. Setien-Fernandez, R.B. Perez-Saez, C. Prieto, R. Escobar Galindo, M. J. Tello, Importance of the spectral emissivity measurements at working temperature to determine the efficiency of a solar selective coating, Sol. Energy Mater. Sol. Cell. 140 (2015) 249–252, https://doi.org/10.1016/j.solmat.2015.04.009.
[49] I. Gonzalez de Arrieta, T. Echaniz, R. Fuente, E. Rubin, R. Chen, J.M. Igartua, M. J. Tello, G.A. Lopez, Infrared emissivity of copper-alloyed spinel black coatings for concentrated solar power systems, Solar Energy Materials and Solar Cells, Sol. Energy Mater. Sol. Cell. 200 (2019) 9, https://doi.org/10.1016/j.solmat.2019.109961, 109961.
[50] E. Le Baron, O. Raccurt, P. Giraud, M. Adier, J. Barriga, B. Diaz, P. Echegut, D. De Sousa Meneses, D. Sciti, A. Soum-Glaude, C. Escape, I. Jerman, G.A. Lopez, T. Echaniz, M.J. Tello, F. Matino, A. Maccari, I. Mercatelli, E. Sani, Round Robin Test for the comparison of spectral emittance measurement apparatuses, Sol. Energy Mater. Sol. Cell. 191 (2019) 476–485, https://doi.org/10.1016/j.solmat.2018.11.026.
[51] OMT solution BV. https://omtsolutions.com/, 2021. (Accessed 28 July 2021).
[52] Surface Optics Corp, 410-Vis-IR portable emissometer & solar reflectometer. https://surfaceoptics.com/products/reflectometers-emissometers/410-vis-ir/, 2021. (Accessed 28 July 2021).
[53] Surface Optics Corp, 10-Solar visible/NIR portable reflectometer. https://surfaceoptics.com/products/reflectometers-emissometers/solar-absorptance-measurements-410/, 2021. (Accessed 28 July 2021).
[54] Surface Optics Corp, ET-100 thermal handheld emissometer. https://surfaceoptics.com/products/reflectometers-emissometers/et100-thermal-hand-held-emissometer/, 2021. (Accessed 28 July 2021).
[55] AZ Technology, TEMP 2000A, Portable Emissometer/Reflectometer, http://www.aztechnology.com/products/reflectometers-and-emissometers/temp-2000a.html [accessed 28/07/2021].
[56] K. Lauder, Spacecraft Thermal Control Coatings and References, NASA Technical Report, NASA/TP, 2005, p. 212792. http://www.aztechnology.com/wp-content/uploads/PDFs/NASA-TP-2005-212792-Lauder.pdf. (Accessed 28 July 2021).
[57] Devices and Services Company, Emissometer model AE1 and RD1 voltmeter. https://www.devicesandservices.com/AE1%20RD1%20Spec%20Sheet.pdf, 2021. (Accessed 28 July 2021).
[58] T.G. Kollie, F.J. Weaver, D.L. McElroy, Evaluation of a commercial, portable, ambient-temperature emissometer, Rev. Sci. Instrum. 61 (1990) 1509–1517, https://doi.org/10.1063/1.1141162.
[59] Labsphere Inc, Technical guide: reflectance materials and coatings, 26, https://www.labsphere.com/site/assets/files/2553/a-guide-to-reflectance-materials-and-coatings.pdf, 2021. (Accessed 28 July 2021).
[60] ASTM International, Standard Tables for Reference Solar Spectral Irradiances: Direct Normal and Hemispherical on 37° Tilted Surface, ASTM G173:2012, 2020, p. 21, https://doi.org/10.1520/G0173-03R20.
[61] National Renewable Energy Laboratory, SMARTS: simple model of the atmospheric radiative transfer of sunshine. https://www.nrel.gov/grid/solar-resource/smarts.html, 2021. (Accessed 28 July 2021).
[62] S. Pratesi, E. Sani, M. De Lucia, Optical and structural characterization of nickel coatings for solar collector receivers, Int. J. Photoenergy (2014) 7, https://doi.org/10.1155/2014/834128, 834128.
[63] S. Pratesi, M. De Lucia, M. Meucci, E. Sani, Structural and optical properties of copper-coated substrates for solar thermal absorbers, Supperlattices and Microstructures 98 (2016) 342–350, https://doi.org/10.1016/j.spmi.2016.08.031.
[64] F. Buendia-Martinez, A. Fernandez-Garcia, F. Sutter, L. Martinez-Arcos, T.J. Reche-Navarro, A. Garcia-Segura, L. Valenzuela, Uncertainty study of reflectance measurements for concentrating solar reflectors, IEEE Trans. Instrum. Meas. 69 (9) (2020) 15, https://doi.org/10.1109/TIM.2020.2975387.